



Influence of Heat Treatment on the Microstructure and Hardness of 17-4PH Stainless Steel Fabricated Through Direct Energy Deposition

Woong Choo¹ · Marzieh Ebrahimian¹ · Kyunsuk Choi² · Jeoung Han Kim¹

Received: 25 July 2022 / Accepted: 19 October 2022

© The Author(s) under exclusive licence to The Korean Institute of Metals and Materials 2022

Abstract

AISI 630 stainless steel (ASTM A564-89, 17-4PH) is widely used in die-casting molds owing to its excellent wear and heat resistance. Recently, a cooling strengthening technology that densifies the microstructure of the casting through rapid cooling has been developed. Additive manufacturing can be used to fabricate casting molds with complex three-dimensional cooling channels. 17-4PH stainless steel, a martensitic precipitation hardening steel, can be subjected to heat treatment to improve its mechanical properties, which are highly dependent on its microstructure. Specifically, the formation of martensite and δ -ferrite, and the coarsening of Cu-rich precipitates considerably decreases the hardness of 17-4PH stainless steel. In this study, we investigate the microstructural evolution of 17-4PH stainless steel during aging and solution heat treatment processes and determine their effect on the formation of martensite and δ -ferrite. Furthermore, the effect of heat treatment on the microstructure and hardness of the steel is studied experimentally. Accordingly, three specimens—as-built, H-1150-M (aging heat treatment), and SH-1150-M (solution and aging heat treatment)—were analyzed and compared herein. The results revealed that the martensite fraction was the highest in the aged H-1150-M specimen, resulting in a high hardness. In contrast, in the SH-1150-M specimen, the austenite and δ -ferrite fractions were higher than the martensite fraction, resulting in a lower hardness than those of the other two specimens. Therefore, aging heat treatment without solution heat treatment can effectively increase the hardness of additively manufactured 17-4PH stainless steel.

Keywords 17-4PH stainless steel · Direct energy deposition · Heat treatment · Hardness · Casting mold · Microstructure

1 Introduction

AISI 630 (17-4PH) stainless steel is a martensitic precipitation hardening alloy with excellent corrosion resistance and good workability compared to other stainless steels [1, 2]. Owing to these properties, it is widely used in the petrochemical, petroleum, paper, dairy, and food processing industries where corrosion resistance is required, as well as for specific applications such as in boat shafts. It is also used for various high strength applications, such as in aircraft parts and other aerospace equipment [3, 4]. The pistons used

in automobile engines must have minimal internal defects to minimize the risk of damage in harsh working environments. Consequently, they are manufactured using gravity casting, which provides relatively good defect control. Pistons are generally mass-produced by using casting molds to ensure high productivity. As 17-4PH stainless steel has excellent wear and heat resistance, it is widely used in piston casting molds [5].

Recently, researchers established a novel cooling strengthening technology that densifies the microstructure of the casting through rapid cooling of the mold [5, 6]. Based on this technique, a method for accelerating the cooling rate by machining a cooling core inside the mold was studied by Ponnusamy et al. [6]. However, in the case of molds fabricated using CNC machining—a conventional manufacturing method—only simple linear cooling water/flow paths can be installed in the cooling core owing to the limitations of the processing methods and tools. Consequently, the final product has a nonuniform structure [7]. Additive manufacturing

✉ Marzieh Ebrahimian
mrzy.ebrahimian@gmail.com

✉ Jeoung Han Kim
jh.kim@hanbat.ac.kr

¹ Department of Materials Science and Engineering, Hanbat National University, Daejeon 34158, Republic of Korea

² Faculty of Industry-Academic Convergence, Hanbat National University, Daejeon 34158, Republic of Korea

can be used to implement an optimized cooling channel inside the mold to maximize the cooling effect.

Additive manufacturing of 17-4PH stainless steel molds with complex cooling core structures is yet to be systematically studied. In particular, as mold materials must have a high wear resistance, the hardness improvement derived through heat treatment must be studied as well. However, there are few studies on the effects of heat treatment on additively manufactured 17-4PH stainless steel. Notably, unlike conventional castings or wrought materials, 17-4PH stainless steel with multilayer molding has a high nonequilibrium austenitic fraction and low hardness [2].

In this study, we investigate the effects of different heat treatment methods for improving the hardness of 17-4PH stainless steel for multilayer molding applications. Accordingly, 17-4PH stainless steel specimens were fabricated through direct energy deposition (DED), and the properties of the as-built specimen were compared with those of heat-treated specimens. Conventionally, solution heat treatment is performed before aging treatment; however, thermal distortion may occur because of nonuniform local shrinkage [8]. Thermal deformation has the opposite effect on near net shape products, offsetting the advantages of the DED production method. Therefore, we also investigate the impact of aging treatment on specimens that are not subjected to heat treatment after DED.

2 Materials and Methods

Commercial 17-4PH stainless steel powder with a nominal composition of Fe_{65.81}-Cr_{17.8}-Ni_{12.8}-Mo_{2.36}-Mn_{1.23} (in wt%) was used herein. The powder was procured from Carpenter Additive (UK) and had a diameter of 61 μm . The scanning electron microscopy (SEM) image and particle size distribution of the powder are shown in Fig. 1a, b, respectively. The chemical composition of the powder was analyzed using inductively coupled plasma optical emission spectroscopy (ICP-OES) and compared to the ASTM A564/A564M [9] material standard, as shown in Table 1. DED was performed with the following parameters: the maximum laser power was set to 210 W, as laser powers above 210 W generated fumes within the Ar operating environment; the maximum laser scanning speed was 480 mm min⁻¹, which ensured proper melting. Specimens with a width, length, and height of 3 mm, 20 mm, and 30 mm, respectively, were fabricated on the 17-4PH stainless steel substrate. The operating conditions of the ICP-OES analysis were as follows: plasma flow rate = 7.5 L min⁻¹, powder carrier gas flow rate = 1.8 L min⁻¹, and powder feed rate = 5 g min⁻¹.

Two specimens were subjected to different heat treatment methods. The H-1150-M specimen was subjected to aging heat treatment at 760 °C (1400 °F) for 2 h followed by 621 °C (1150 °F) for 4 h, whereas the SH-1150-M specimen was subjected to solution annealing at 1038 °C (1900

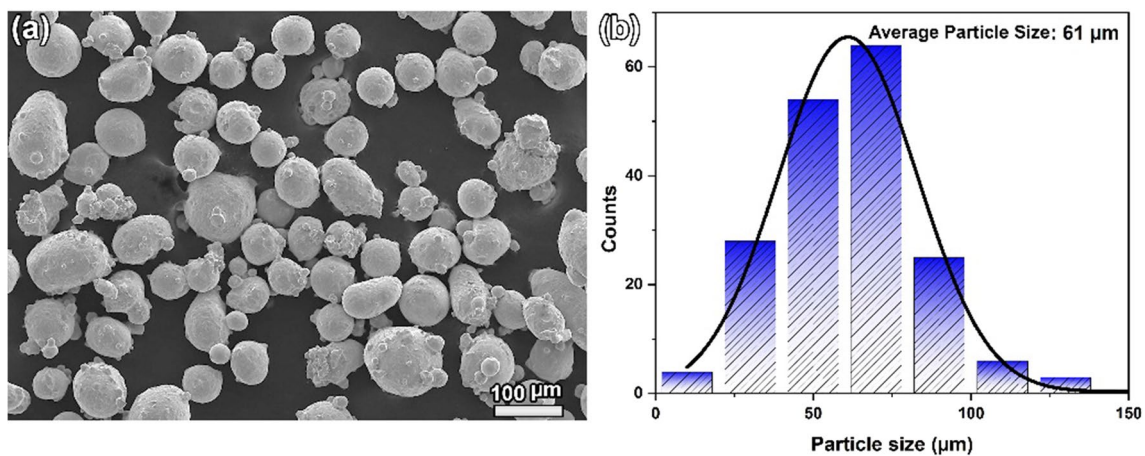


Fig. 1 a SEM image and b particle size distribution of 17-4PH stainless steel powder

Table 1 Chemical composition of the as-received 17-4PH stainless steel powder compared to the ASTM specifications for 17-4PH stainless steel (wt%)

Component	Fe	Cr	Ni	Cu	Mn	Nb	O	N
As-received powder	Bal	15.50	4.58	4.54	0.34	0.24	105 ppm	770 ppm
ASTM 17-4PH [9]	Bal	15–17.50	3–5	3–5	≤1	≤0.45	–	–

°F) for 1 h and then aged at 760 °C (1400 °F) for 2 h and 621 °C (1150 °F) for 4 h. Both specimens were naturally air-cooled to 25 °C after their respective heat treatments. The H-1150-M specimen is resistant to thermal shock as 17-4PH stainless steel has high flexibility after heat treatment [10]. 17-4PH stainless steel also has good oxidation resistance. However, extended exposure of grades 630–370 to temperatures above 480 °C should be avoided to prevent a loss in toughness at ambient temperatures. Furthermore, these steel grades should not be used at temperatures above the age-hardening temperature as this may reduce the hardness and mechanical properties of the metal. Therefore, 17-4PH stainless steel is age-hardened at low temperatures to achieve the required mechanical properties. The two heat treatment methods used herein are summarized in Table 2. The microstructure and mechanical properties of the two heat-treated specimens were compared with those of the as-built specimen (without heat treatment).

Test specimens were cut from the bulk specimens using electro-discharge machining followed by mounting, grinding, polishing, and etching in Kalling's solution composed of 50 mL HCl + 100 mL ethanol + 50 g CuCl₂. The microstructure of the specimens was characterized through optical (OLYMPUS GX41 model, Japan) and scanning electron microscopy (Oxford X-MAX) with electron backscatter diffraction (EBSD; JSM-7100F, Japan). The hardness of the specimens was evaluated using a micro-hardness tester (Duramin-40 Struers) under a load of 100 kgf (980 N) for 10 s. To investigate the evolution of the microstructure, the specimens were mechanically ground to 0.25 mm in a diamond suspension and electropolished in a solution containing 78 mL phosphoric acid, 90 mL distilled water, and 100 mL botoxyethanol for 60 s. The phases and crystal-line structure of the specimens were characterized through X-ray diffraction (XRD; SmartLab model, Japan) using Cu-K α radiation ($\lambda = 1.54056$ Å, 2θ ranging from 10° to 120°, step size of 0.02 µm, and dwell time of 1 s per step) at an operating voltage of 40 keV and a current of 300 mA.

Table 2 Heat treatment methods (H=aging treatment, S=solution treatment)

Specimen	Heat treatment methods	
	Solution treatment	Aging treatment
As-built	N/A	N/A
H-1150-M	N/A	760 °C (1400 °F) for 2 h followed by 621 °C (1150 °F) for 4 h and air cooling
SH-1150-M	1038 °C (1900 °F) for 1 h followed by air cooling	760 °C (1400 °F) for 2 h followed by 621 °C (1150 °F) for 4 h and air cooling

The diffraction spectra were analyzed through the Rietveld method using the Materials Analysis Using Diffraction software. In the Rietveld refinement method, parameters such as peak position and peak symmetry are calibrated with respect to a standard sample (Si powder herein). The diffraction pattern is then simulated using a series of structural parameters, such as peak shape, width, and background parameters. Subsequently, the data are fit using the least-squares method. A detailed description of this analysis method is available in [11, 12]. The sizes and distributions of the precipitates were determined using transmission electron microscopy (TEM, HITACHI HF5000, Japan) at 200 kV. TEM specimens were prepared using a focused ion beam system (nx5000, Japan).

3 Results

3.1 Microstructural Analysis

Aging treatment is an effective method of enhancing the mechanical properties of a material owing to the precipitation of fine precipitates in the matrix. The microstructures of the fabricated specimens, both before and after aging/solution heat treatments, were analyzed using an optical microscope. The optical images of the specimens (as-built, H-1150-M, and SH-1150-M) are shown in Fig. 2. As shown in Fig. 2a, the microstructure of the as-built specimen comprised austenite and martensite phases. Herein, the austenite and martensite phases are referred to as the face-centered cubic (FCC) and body-centered cubic (BCC) phases, respectively. The structure shown in Fig. 2a is consistent with the microstructure of additively manufactured specimens. Notably, the as-built specimen, which was fabricated through DED herein, had a finer structure than conventional melted/forged specimens [13]. In addition, a “fish-scale” type melt pool structure, which is typical in additively manufactured materials, can be observed in Fig. 2a (indicated by the white dashed lines). The microstructure of the H-1150-M specimen is shown in Fig. 2b. After heat treatment, the fish-scale-like structure disappeared; the retained austenite and martensite laths (marked by a red circle in Fig. 2b) and 6% volume fraction of δ -ferrite (indicated by a white arrow in the matrix) are observed. Owing to martensite tempering, the lath boundaries and existing austenitic grain boundaries are visible in the SEM images. Regardless of the heat treatment conditions, the martensite thickness in 17-4PH stainless steel depends on the location of the molten pool (the bottom of the pool or adjacent to the heat-affected zone), owing to the austenite transformation caused by the heat generated in the subsequent layers [14, 15].

Nanosized spheroidal Cu precipitates, which are typical in precipitation hardening steel, are formed and dispersed in the martensite blocks. In general, solution treatment

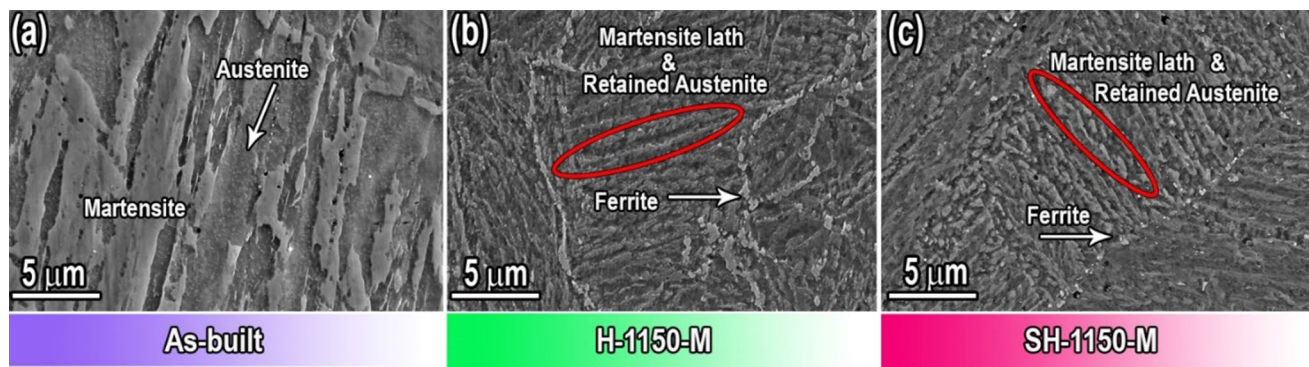


Fig. 2 SEM images of DED fabricated specimens: **a** as-built; **b** H-1150-M; and **c** SH-1150-M

Table 3 Chemical composition of the printed specimens (as-built, H-1150-M, and SH-1150-M)

Component	Cr	Ni	Cu	Mn
As-built	15.1	5.5	6.1	0.53
H-1150-M	13.1	4.6	5.1	0.45
SH-1150-M	13.1	4.6	5.1	0.45

affects the effective grain size, mechanical properties, and subsequent aging strengthening of additively manufactured materials. The microstructure of the SH-1150-M specimen is shown in Fig. 2c. The solution-aged 17-4PH stainless steel is composed of a large fraction of retained austenite and martensite laths and a small fraction of δ -ferrite (0.9%), as observed in Fig. 2c. As shown, the volume fraction of austenite increased during high-temperature solution annealing, and a considerable amount of prior-austenite was present at the grain boundaries.

The chemical composition (ICP-OES results) of the printed specimens (as-built, H-1150-M, and SH-1150-M) is listed in Table 3.

3.2 XRD Analysis

The XRD patterns obtained at different locations, namely, the top, middle, and bottom of the three manufactured specimens, are shown in Fig. 3. The XRD patterns of the as-built, H-1150-M, and SH-1150-M specimens are shown in Fig. 3a–f, respectively. The XRD patterns revealed that all the specimens contained BCC (martensite or ferrite phase, α) and FCC (austenite phase, γ) phases. Notably, XRD cannot be used to distinguish between ferrite and martensite as they occupy the same 2 θ positions. In the as-built specimen, BCC refers only to the martensite phase as 17-4PH stainless steel is a martensitic precipitation hardening alloy. However, in the other two specimens (H-1150-M and SH-1150-M) BCC refers to both the ferrite and martensite phases. In all

three specimens, (110) BCC was dominant, and (111) FCC had a low intensity. The enlarged rectangular area between 42° and 52° shown in Fig. 3b, d, f exhibits a decrease in the (011) peak intensity corresponding to the BCC phase from the lower to the upper layers of the specimens which may be attributed to the textural evolution caused by the evolution of the martensitic microstructure. Furthermore, as shown in Fig. 3b, d, f, the position of the (011) peak did not shift to lower or higher Bragg angles from the lower to the upper layers, which indicates that the degree of lattice distortion in the alloys during the heat treatment is negligible.

The diffraction spectra were analyzed using the Rietveld method to quantify the BCC and FCC phase fractions. The FCC and BCC phase fractions and their lattice parameters at different locations (top, middle, and bottom) on the specimens are summarized in Table 4. The volume fraction of the BCC phase at the bottom, middle, and top of the as-built specimen was 79.5%, 82.5%, and 86.1%, respectively. After aging treatment, the volume fraction of the BCC phase increased to 85%, 86.5%, and 87.6% at the bottom, middle, and top, respectively, of the H-1150-M specimen. In contrast, the volume fraction of the BCC phase decreased to 70%, 76%, and 78% at the bottom, middle, and top, respectively, of the SH-1150-M specimen. The results shown in Table 4 reveal that the BCC phase fraction in the upper layers of the specimens is higher than that in the lower layers. This suggests that austenite transformation is more accessible in the lower layers owing to heat transfer from the upper layers [16]. The lattice parameters of the FCC/BCC phases were calculated to be 3.596/2.875 Å, 3.590/2.871 Å, and 3.592/2.871 Å in the as-built, H-1150-M, and SH-1150-M specimens, respectively.

3.3 Effect of heat treatment on hardness

The effect of heat treatment on the hardness of the specimens in different zones (top, middle, and bottom) along the DED stacking direction was investigated herein (Fig. 4).

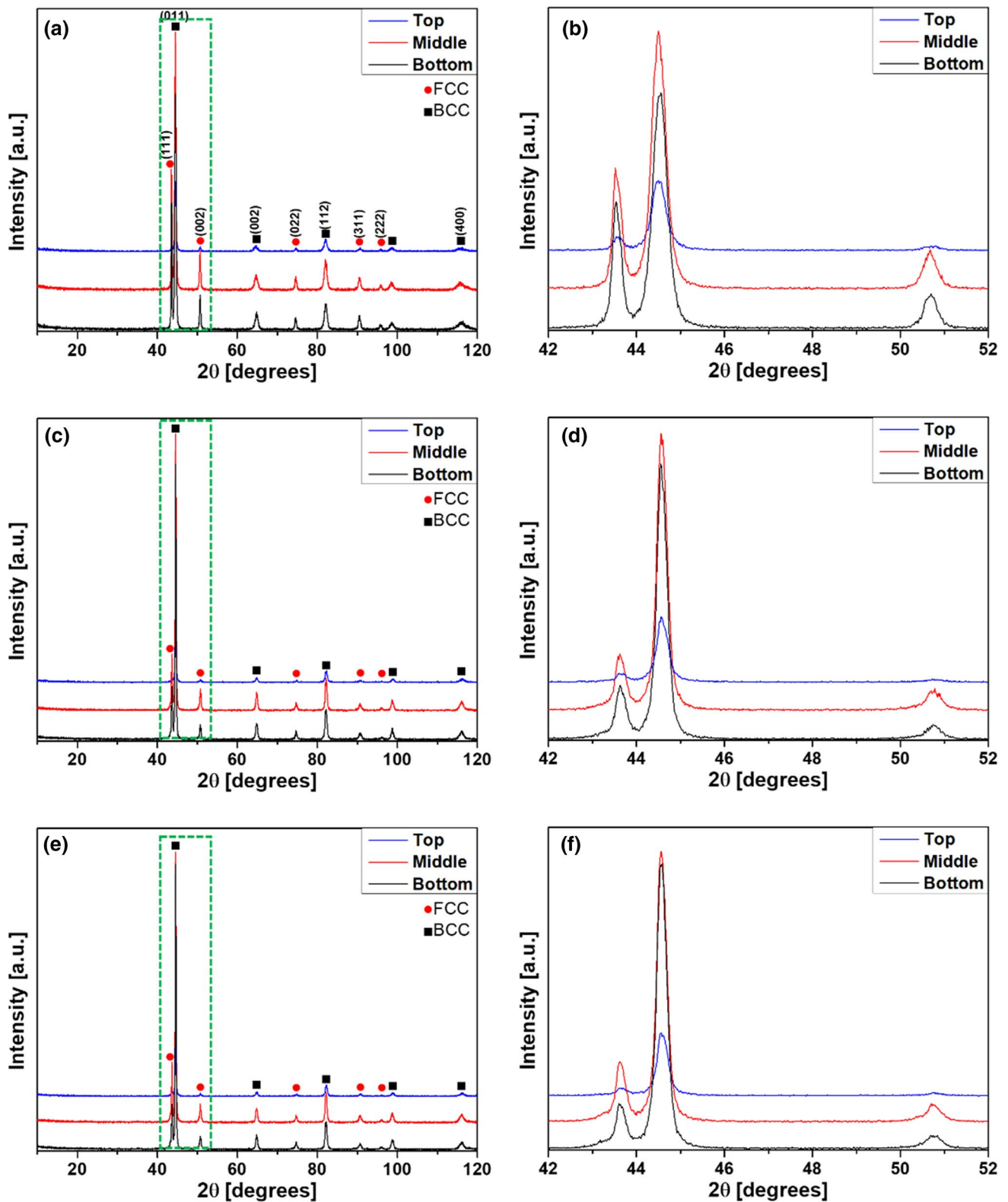


Fig. 3 XRD plots of the top, middle, and bottom of: **a** as-built specimen, with **b** partially enlarged XRD pattern between 42° and 52° of as-built specimen; **c** H-1150-M specimen, with **d** partially enlarged

XRD pattern between 42° and 52° of H-1150-M specimen; and **e** SH-1150-M specimen, with **f** partially enlarged XRD pattern between 42° and 52° of SH-1150-M specimen

Table 4 Phase volume fraction and lattice parameters of each phase determined through Rietveld analysis of the XRD patterns

Specimen	Top			Middle	Bottom
As-built	BCC	a_{bcc}	2.875 Å	2.877 Å	2.877 Å
		f_{bcc}	79.5%	82.5%	86.1%
	FCC	a_{fcc}	3.597 Å	3.597 Å	3.595 Å
		f_{fcc}	20.5%	17.5%	13.9%
H-1150-M	BCC	a_{bcc}	2.873 Å	2.872 Å	2.870 Å
		f_{bcc}	85%	86.5	87.6%
	FCC	a_{fcc}	3.592 Å	3.592 Å	3.588 Å
		f_{fcc}	15%	13.5%	12.4%
SH-1150-M	BCC	a_{bcc}	2.872	2.873 Å	2.870 Å
		f_{bcc}	70%	76%	78%
	FCC	a_{fcc}	3.592 Å	3.592 Å	3.592 Å
		f_{fcc}	30%	24%	22%

a_{phase} and f_{phase} represent the lattice parameter and phase volume fraction, respectively, of the given phase

The hardness in different zones is illustrated by the dotted vertical lines in Fig. 4. The average hardness of the as-built specimen was 354 HV (Fig. 4a). After aging heat treatment (H-1150-M), the average hardness increased to 361 HV (Fig. 4b) owing to the formation of Cu-rich zones, which occur before Cu precipitation [1]. After solution annealing and aging treatment (SH-1150-M), the average hardness decreased to 341 HV (Fig. 4c) owing to the decrease in the volume fraction of martensite coupled with the formation of δ -ferrite in the microstructure and the presence prior-austenite at the grain boundaries. Moreover, the hardness also decreased owing to precipitate coarsening and martensite tempering during the solution annealing and aging treatment.

The hardness increased from the lower to the upper layers of the additively manufactured specimens [17, 18]. In the DED method, as the height of the specimen increases, the

cooling rate decreases, and larger amounts of Cu are precipitated owing to prolonged exposure to the aging temperature [19]. Notably, a direct relationship exists between the volume fraction of the BCC phase and the hardness of the specimen: as the volume fraction of the BCC phase increases, the hardness increases. As the height of the specimen increases, martensite transformation occurs in the lower layers owing to heat transfer from the upper layers. Therefore, the volume fraction of the BCC phase increases from the bottom to the top of the specimens. Consequently, the hardness increases with the increase in height. The H-1150-M specimen has the highest BCC volume fraction: BCC includes both the ferrite and martensite phases (Sect. 3.1) and the microstructure of the H-1150-M specimen has a higher δ -ferrite volume fraction (6%) than that of the SH-1150-M specimen (0.9%) (Sect. 3.1). As the H-1150-M specimen had the highest hardness, it can be inferred that most of BCC phase in this specimen is the martensite phase.

3.4 EBSD Analysis

The effect of heat treatment processing on the microstructural evolution of the specimens was analyzed by systematically investigating their substructures using EBSD. The EBSD phase map, inverse pole figure (IPF) map, and kernel average misorientation (KAM) map of the lower, middle, and upper layers of the as-built, H-1150-M, and SH-1150-M specimens are shown in Figs. 5a–c, 6a–c, and 7a–c, respectively. As shown in the phase maps in Fig. 5a, the microstructure of the lower, middle, and upper layers of the as-built specimen consisted of both FCC and BCC phases. The IPF maps shown in Fig. 4b show that the grains formed parallel to the heat transfer direction. The microstructure of the as-built specimen was composed of fine and large grains, wherein the fine grains were primarily the BCC phase and the large grains were the FCC phase. The average grain sizes of the FCC and BCC phases determined by

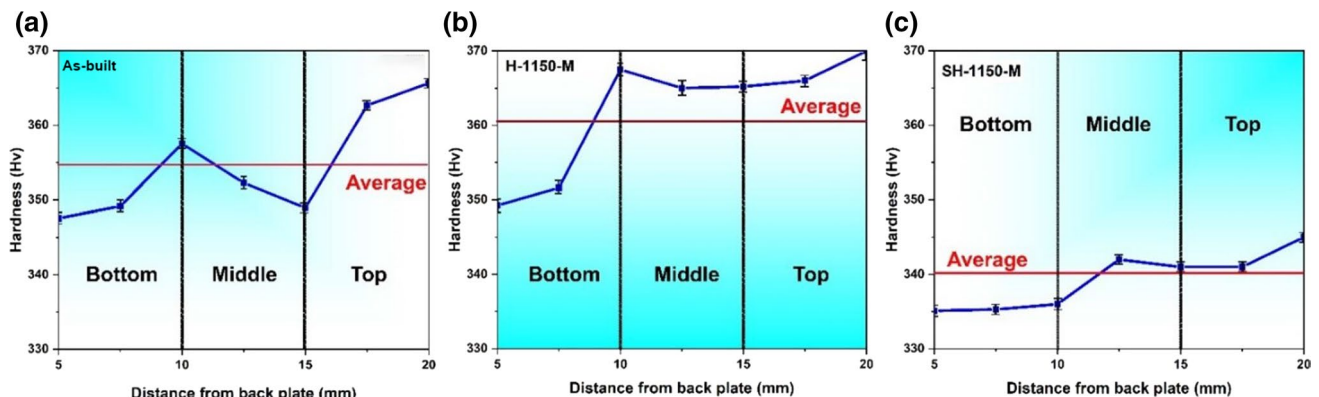


Fig. 4 Distribution of Vickers hardness from bottom to top of: **a** as-built specimen; **b** H-1150-M specimen; and **c** SH-1150-M specimen

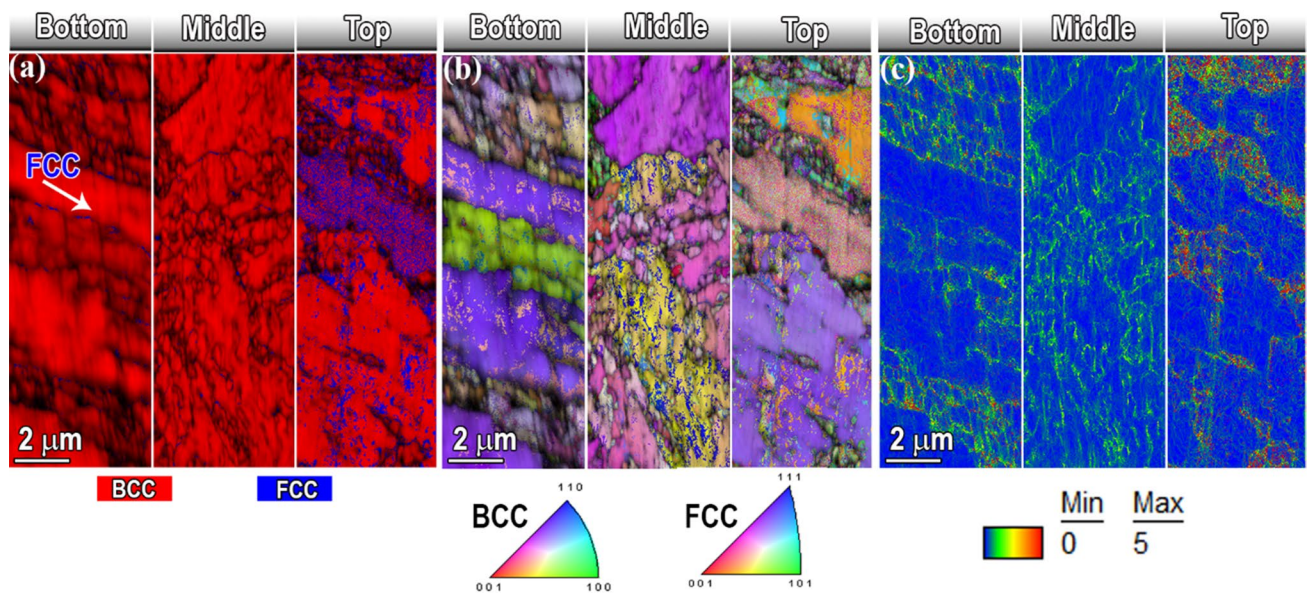


Fig. 5 **a** EBSD phase map, **b** IPF map, and **c** KAM map taken from the lower, middle, and upper layers of the as-built specimen

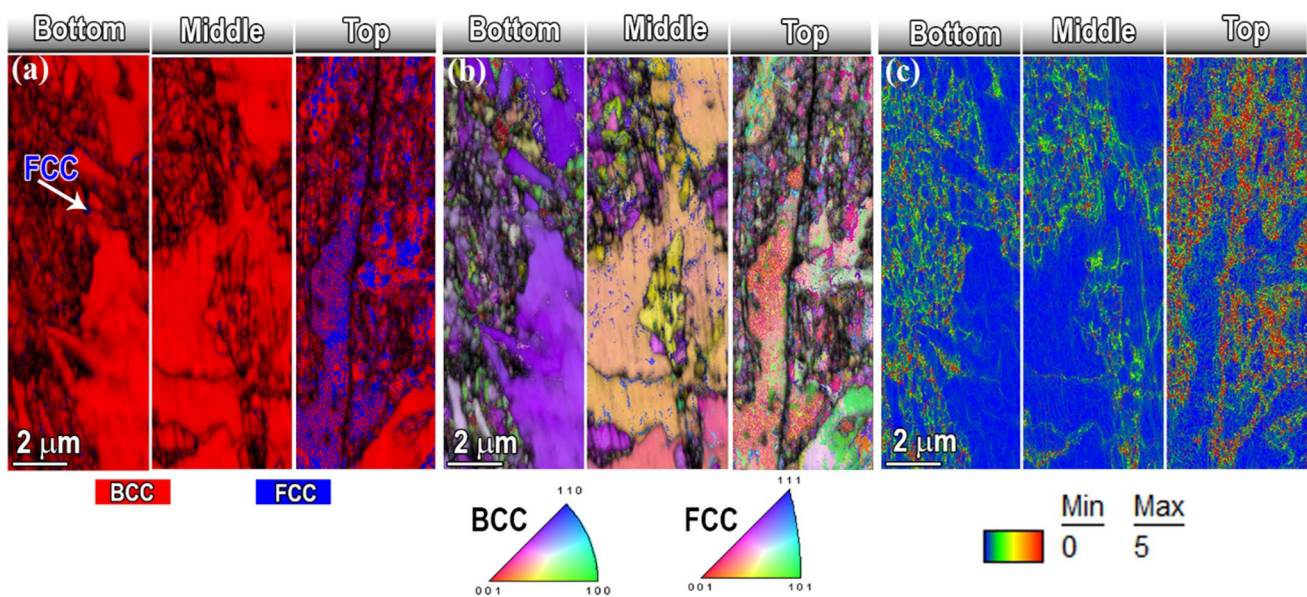


Fig. 6 **a** EBSD phase map, **b** IPF map, and **c** KAM map taken from the lower, middle, and upper layers of the H-1150-M specimen

EBSD were 2.2 μm and 1.3 μm , respectively. The columnar BCC grains parallel to the building plane have a relatively strong texture compared to the equiaxed grains at the top of the specimens. This textural evolution is in good agreement with the XRD results shown in Fig. 3 wherein the intensity of the (011) peak decreases from the lower to the upper layers in accordance with the decrease in the BCC phase. The KAM map (Fig. 5c) indicates that a high KAM value exists near the junctions of the FCC and BCC phases. Owing to the

transformation of martensite to austenite, the local strain at the junction of these phases increases.

The EBSD images of the H-1150-M specimen are shown in Fig. 6. The phase map of the lower, middle, and upper layers of the aged specimen is shown in Fig. 6a. As shown, this specimen also contains two phases: FCC and BCC. The percentage of the FCC phase in the upper layer is significantly higher than that in the as-built specimen, reaching 33%. The IPF map in Fig. 6b shows the formation of a heterogeneous

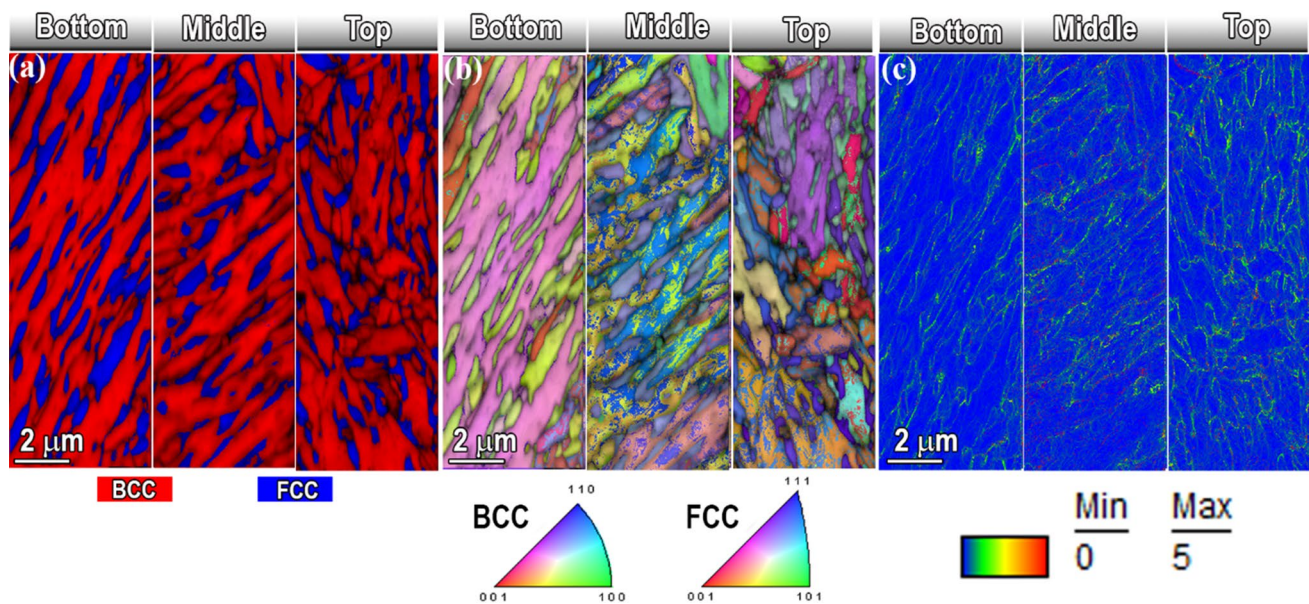


Fig. 7 **a** EBSD phase map, **b** IPF map, and **c** KAM map taken from the lower, middle, and upper layers of the SH-1150-M specimen

bimodal structure containing large BCC grains with an average grain size of 3 μm and smaller BCC grains with an average grain size of 0.3 μm . This can be attributed to static recrystallization during the aging process. However, the aging temperature and time were insufficient to complete the static recrystallization process, and the structure was only partially recrystallized. The KAM map in Fig. 6c demonstrates that the KAM values at the interface between the large and small grains are high, which may be attributed to the accumulation of dislocations behind the grain boundaries during static recrystallization through the bulging process.

The EBSD images of the SH-1150-M specimen are shown in Fig. 7. As shown in the EBSD phase map of this specimen (Fig. 7a), the volume fractions of the FCC phase in the lower, middle, and upper layers are 3%, 18%, and 45%, respectively. The IPF map in Fig. 7b shows that the grain size increased to 6 μm in the upper layers, and the FCC volume fraction increased as well. The KAM map (Fig. 7c) shows that the KAM values in the SH-1150-M specimen are significantly lower than those in the as-built and H-1150-M specimens, which can be attributed to the completion of the static recrystallization process and the grain coarsening that occurs during the solution annealing and aging treatment.

3.5 Cu Precipitation

The specimens were investigated by TEM to determine the relationship between their microstructures and mechanical properties with respect to different heat treatment processes. The TEM images and the corresponding elemental EDS maps of the H-1150-M and SH-1150-M specimens

are shown in Fig. 8. The TEM-EDS maps of the H-1150-M specimen in Fig. 8a reveal a homogeneous distribution of nanosized Cu-rich precipitates in the matrix, with an average size of 22 nm. The SH-1150-M specimen has coarser but a fewer Cu-rich particles than the H-1150-M specimen, as shown in Fig. 8b (60 nm). Nanosized precipitates can function as a strong barrier against dislocation motion and improve the mechanical properties of the alloy. The size, strength, and distribution of precipitates are key parameters that affect the precipitate strengthening of metals and alloys [1]. Therefore, the H-1150-M specimen has a higher hardness than the SH-1150-M specimen because of the precipitation and uniform distribution of nanosized Cu-rich particles, which strengthen the alloy via Orowan strengthening effect. The difference between the Vickers hardness of the specimens in Fig. 4 is attributed to this effect [19].

4 Discussion

Precipitation hardening 17-4PH stainless steel combines high strength and hardness with good corrosion resistance. The increase in strength in this precipitation hardening stainless steel can be attributed to the combination of the Cu precipitation phase over several nanometers and the martensitic structure. After DED, a high amount of austenite persists in the bulk material. Solution heat treatment at 1038 $^{\circ}\text{C}$ (which exceeds the transition temperature of 727 $^{\circ}\text{C}$) reverts martensite (α') to the parent austenite (γ) phase and omits residual stresses [20]. A reverse transformation from austenite (γ) to martensite (α') occurs as the

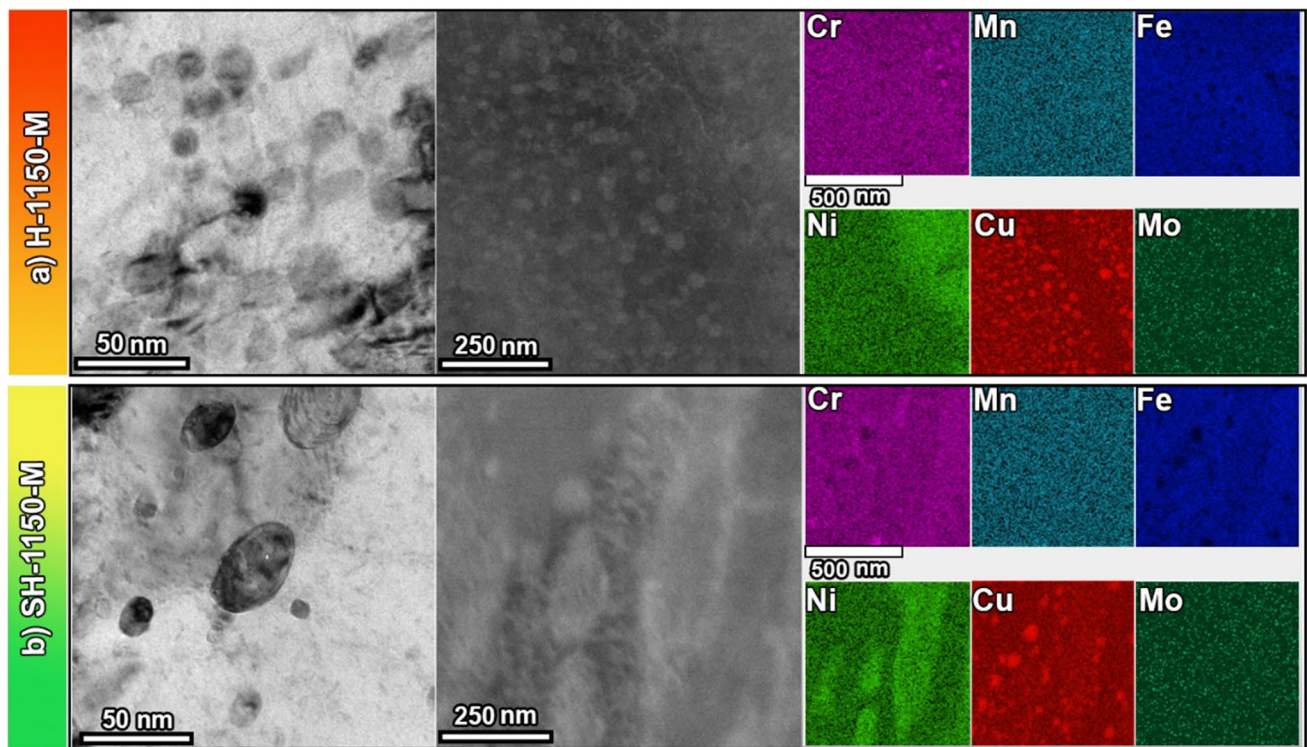


Fig. 8 Comparison of TEM-EDS results of 17-4PH stainless steel: **a** H-1150-M specimen and **b** SH-1150-M specimen

steel cools to the ambient temperature, with the transformation starting (M_s) at approximately 100 °C and ending (M_f) at approximately 32 °C. The aging treatment results in the nucleation and growth of Cu-rich precipitates that increase in size with the increase in time and temperature. Martensite can be converted to austenite by the diffusion-controlled segregation of stabilizing and substitutional elements during the aging treatment process. Austenite grains nucleate at the boundaries of the lath and parent austenite [21]. As M_f is close to the room temperature, the retained austenite has a high solubility of Cu, which prevents the formation of a Cu precipitation phase after aging. Therefore, the overall strength is reduced. In particular, laminated specimens experience a high level of residual stress formation, which suppresses martensite formation. Martensitic precipitation hardening steels, of which 17-4PH is the most common grade, transform to martensite at low temperatures, typically at approximately 250 °C. The aging heat treatment temperature used herein was 621 °C, which exceeds the martensitic transformation temperature. Therefore, owing to the metastability of austenite at 621 °C, the percentage of martensite increases. The solubility of Cu is higher in the austenite grains than in the martensite grains, and Cu does not precipitate during the heat treatment process. Furthermore, aging at 621 °C strengthens the alloy and relieves the residual thermal stresses [22]. As a result, austenite transforms

into martensite during cooling. The XRD analysis clearly demonstrates this reduced austenite volume fraction in the H-1150-M specimen. In addition, the metastable martensite in H-1150-M decomposes to austenite during aging heat treatment. After cooling to room temperature, the austenite grains return to stable lath martensite without the accompanying segregation of austenite stabilizing elements. In contrast, solution and aging heat treatment increase the residual stress generated during lamination and decrease the strength of the alloy, with an increase in the possibility of cracking or distortion. Therefore, solution heat treatment is not recommended after aging heat treatment. In the case of a wrought material, a low austenite fraction is retained if the SH-1150-M heat treatment process is performed. In particular, owing to the characteristics of martensitic corrosion resistant stainless steel, a high fraction of the BCC phase can be obtained despite air cooling. However, when the SH-1150-M heat treatment process is performed on additively manufactured specimens, the martensitic structure disappears, and a mixed composition of ferrite and austenite is obtained, as shown in Figs. 2 and 5. Accordingly, the average hardness decreases to 340 HV. In the case of the as-built specimen, the transformation from δ -ferrite to austenite becomes difficult owing to the quenching effect, and ferrite becomes the main phase at room temperature. However, during slow cooling after the SH-1150-M heat treatment, some ferrite

transforms into austenite as the temperature passes through the austenite stabilization range [23]. The slower the cooling rate, the higher the volume fraction of austenite. In contrast, in the case of annealed materials, solidification begins with austenite, which transforms to martensite, and consequently, martensite is the main phase at room temperature [24].

5 Conclusions

This study examined the effects of different heat treatment methods on the mechanical properties and microstructure of 17-4PH stainless steel that was fabricated through DED. In addition, the metallography and hardness of the prepared 17-4PH stainless steel specimens were analyzed. The following conclusions were drawn.

1. The microstructure of the as-built specimens comprises austenite and martensite phases with “fish-scale” structures. The fish-scale-like structures disappear after aging treatment (H-1150-M), and austenite and martensite laths are retained. The aging heat treatment transforms austenite and δ -ferrite to martensite, which is the dominant phase. Furthermore, nanosized spheroidal Cu precipitates are formed and dispersed in the martensite blocks.
2. After solution annealing (SH-1150-M), the precipitation becomes coarse and martensite formation is tempered. The higher the annealing temperature, the higher the volume fraction of austenite and δ -ferrite. A significant amount of prior-austenite was also observed at the grain boundaries in optical microscopic images.
3. The XRD patterns of the three specimens (as-built, H-1150-M, and SH-1150-M) clearly showed the FCC (austenite phase, γ) and BCC (martensite or ferrite phase, α) phases. (110) BCC was dominant, and (111) FCC exhibited a low intensity. The phase fraction of BCC in the upper layers of the specimens was higher than that in the lower layers. This is because austenite transformation is more likely in the lower layers owing to heat transfer from the upper layers.
4. The average hardness of the as-built specimen was 354 HV. After aging heat treatment (H-1150-M), the average hardness increased to 361 HV owing to the formation of Cu-rich zones, which occur before Cu precipitation. In contrast, after solution annealing and aging treatment (SH-1150-M), the average hardness decreased to 341 HV owing to the decreasing volume fraction of martensite and the formation of δ -ferrite in the microstructure and prior-austenite at the grain boundaries.
5. As the H-1150-M specimen had the highest hardness, it can be concluded that most of the BCC phase in this specimen is the martensite phase.

Acknowledgements This work was supported by the Industrial Technology Innovation Program (Grant No. 20013122; Development of manufacturing technology for casting molds with 3D cooling channels to improve the quality and productivity of automobile parts) funded by the Ministry of Trade, Industry, and Energy (MOTIE), Republic of Korea. This work was also supported by the Korea Institute for Advancement of Technology (KIAT), funded by the Ministry of Trade, Industry, and Energy (MOTIE), Republic of Korea (Grant No. P0002019; Human Resource Development Program for Industrial Innovation).

Declarations

Conflict of interests The authors have no competing interests to declare that are relevant to the content of this article.

References

1. B. Wang, J. Zhang, W. Zhou, W. Xia, W.J. Deng, *Adv. Mech. Eng.* (2016). <https://doi.org/10.1177/1687814016665745>
2. J. Burja, B. Šuler, A. Nagode, *Materwiss. Werkst.* **50**, 405 (2019). <https://doi.org/10.1002/mawe.201800045>
3. J.D. Bressan, D.P. Daros, A. Sokolowski, R.A. Mesquita, C.A. Barbosa, J. Mater. Process. Tech. **205**, 353 (2008). <https://doi.org/10.1016/j.jmatprotec.2007.11.251>
4. M. Lara-Banda, C. Gaona-Tiburcio, P. Zambrano-Robledo, M. Delgado-E, J.A. Cabral-Miramontes, D. Nieves-Mendoza, E. Maldonado-Bandala, F. Estupiñán-López, J.G. Chacón-Nava, F. Almeraya-Calderón, *Materials* **13**, 2836 (2020). <https://doi.org/10.3390/ma13122836>
5. M. Raza, R. Svenningsson, M. Irwin, *Metall. Foundry Eng.* **41**, 85 (2015). <https://doi.org/10.7494/mafe.2015.41.2.85>
6. P. Ponnusamy, Basant Sharma, S.H. Masood, R.A. Rahman Rashid, Riyan Rashid, S. Palanisamy, D. Ruan, *Mater. Today Proc.* **45**, 4531 (2021). <https://doi.org/10.1016/j.matpr.2020.12.1104>
7. K. Zhuang, X. Zhang, D. Zhu, H. Ding, *Int. J. Adv. Manuf. Technol.* **80**, 1815 (2015). <https://doi.org/10.1007/s00170-015-7153-8>
8. J.K. Kuo, P.H. Huang, H.Y. Lai, J. Adv. Manuf. Technol. **92**, 1093 (2017). <https://doi.org/10.1007/s00170-017-0198-0>
9. ASTM A564/A564M-13, Standard Specification for Hot-Rolled and Cold-Finished Age-Hardening Stainless Steel Bars and Shapes (ASTM International, West Conshohocken, 2017)
10. C. Feng, L. Zhang, J. Wu, H. Yu, *Mater. Res. Express* **7**, 046503 (2020). <https://doi.org/10.1088/2053-1591/ab815f>
11. M.S. Rizi, H. Minouei, B.J. Lee, H. Pouraliakbar, M.R. Toroghinejad, S.I. Hong, *Mater. Sci. Eng. A* **824**, 141803 (2021). <https://doi.org/10.1016/j.msea.2021.141803>
12. M. Saboktakin Rizi, H. Minouei, B.J. Lee, M.R. Toroghinejad, S.I. Hong, *J. Alloys Compd.* **911**, 165108 (2022). <https://doi.org/10.1016/j.jallcom.2022.165108>
13. Y. Sun, R.J. Hebert, M. Aindow, *Mater. Des.* **156**, 429 (2018). <https://doi.org/10.1016/j.matdes.2018.07.015>
14. Y. Sun, R.J. Hebert, M. Aindow, *Mater. Des.* **140**, 153 (2018). <https://doi.org/10.1016/j.matdes.2017.11.063>
15. R. Sowa, A. Kowal, E. Roga, S. Arabasz, A. Dziedzic, I. Dul, M. Parlinska-Wojtan, *Zastita Materijala* **56**, 261 (2015). <https://doi.org/10.5937/zasmat1503261s>

16. J.L. Tian, W. Wang, W. Yan, Z. Jiang, Y. Shan, K. Yang, J. Iron Steel Res. Int. **24**, 718 (2017). [https://doi.org/10.1016/S1006-706X\(17\)30108-5](https://doi.org/10.1016/S1006-706X(17)30108-5)
17. N. Kwabena Adomako, S.H. Kim, J.H. Yoon, S.-H. Lee, J.H. Kim, Metals **11**, 629 (2021). <https://doi.org/10.3390/met11040629>
18. D. Guo, K. Yan, M.D. Callaghan, D. Daisenberger, M. Chatterton, J. Chen, A. Wisbey, W. Mirihanage, Mater. Des. **207**, 109782 (2021). <https://doi.org/10.1016/j.matdes.2021.109782>
19. G. Yeli, M.A. Auger, K. Wilford, G.D.W. Smith, P.A.J. Bagot, M.P. Moody, Acta Mater. **125**, 38 (2017). <https://doi.org/10.1016/j.actamat.2016.11.052>
20. T. LeBrun, T. Nakamoto, K. Horikawa, H. Kobayashi, Mater. Des. **81**, 44 (2015). <https://doi.org/10.1016/j.matdes.2015.05.026>
21. N.K. Adomako, J.O. Kim, J.H. Kim, Mater. Sci. Eng. A **753**, 208 (2019). <https://doi.org/10.1016/j.msea.2019.03.036>
22. B. Zheng, J.C. Haley, N. Yang, J. Yee, K.W. Terrassa, Y. Zhou, E.J. Lavernia, J.M. Schoenung, Mater. Sci. Eng. A **764**, 138243 (2019). <https://doi.org/10.1016/j.msea.2019.138243>
23. S. Vunnam, A. Saboo, C. Sudbrack, T.L. Starr, Addit. Manuf. **30**, 100876 (2019). <https://doi.org/10.1016/j.addma.2019.100876>
24. S.D. Meredith, J.S. Zuback, J.S. Keist, T.A. Palmer, Mater. Sci. Eng. A **738**, 44 (2018). <https://doi.org/10.1016/j.msea.2018.09.066>

Publisher's Note Springer Nature remains neutral with regard to jurisdictional claims in published maps and institutional affiliations.

Springer Nature or its licensor (e.g. a society or other partner) holds exclusive rights to this article under a publishing agreement with the author(s) or other rightsholder(s); author self-archiving of the accepted manuscript version of this article is solely governed by the terms of such publishing agreement and applicable law.